ADVANCED FUNCTIONAL MATERIALS
www.afm-journal.de

Few-Layer $MoSe_2$ Nanosheets with Expanded (002) Planes Confined in Hollow Carbon Nanospheres for Ultrahigh-Performance Na-Ion Batteries

Hui Liu, Hong Guo, Beihong Liu, Mengfang Liang, Zhaolin Lv, Keegan R. Adair, and Xueliang Sun**

Sodium-ion batteries (SIBs) are considered as a promising alternative to lithium-ion batteries, due to the abundant reserves and low price of Na sources. To date, the development of anode materials for SIBs is still confronted with many serious problems. In this work, encapsulation-type structured $MoSe_2$@hollow carbon nanosphere (HCNS) materials assembled with expanded (002) planes few-layer $MoSe_2$ nanosheets confined in HCNS are successfully synthesized through a facile strategy. Notably, the interlayer spacing of the (002) planes is expanded to 1.02 nm, which is larger than the intrinsic value of pristine $MoSe_2$ (0.64 nm). Furthermore, the few-layer nanosheets are space-confined in the inner cavity of the HCNS, forming hybrid $MoSe_2$@HCNS structures. When evaluated as anode materials for SIBs, it shows excellent rate capabilities, ultralong cycling life with exceptional Coulombic efficiency even at high current density, maintaining 501 and 471 mA h g^{-1} over 1000 cycles at 1 and 3 A g^{-1}, respectively. Even when cycled at current densities as high as 10 A g^{-1}, a capacity retention of 382 mA h g^{-1} can be achieved. The expanded (002) planes, 2D few-layer nanosheets, and unique carbon shell structure are responsible for the ultralong cycling and high rate performance.

1. Introduction

With the constantly growing demand for high energy and power density energy storage devices, sodium-ion batteries (SIBs) have recently received tremendous attention as an alternative to Li-ion batteries due to the abundant reserves and low price of sodium sources.[1–3] In recent times, reports on cathode materials for Na-ion batteries have shown capability comparable to their Li-ion battery counterparts. However, the large radius of Na^+ (1.02 Å) compared with that of Li^+ (0.76 Å) leads to the inability to use graphite structures for Na-ion batteries.[4–6] Moreover, the development of anode materials for SIBs is still confronted with many serious problems, such as low conductivity, large volume expansions, poor dynamics, low rate performance, unsatisfied cycling life, and inferior capacity.[7–9] Therefore, the major challenge for SIBs resides in designing novel anodes with enhanced electrochemical performance including high reversible capacity, good rate capability, improved stability, and long cycling life. Recently, 2D layered transition metal dichalcogenides (TMDs) have attracted considerable attention in the fields of energy and environmental applications.[10–13] Particularly, MoS_2 has been extensively investigated as a promising material for LIBs and SIBs.[9,14–17] Chen and co-workers prepared petal-like MoS_2@C nanosheets, exhibiting high reversible capacity of about 993 mA h g^{-1} at 1 A g^{-1} after 200 cycles.[18] Nonetheless, when used in SIBs, it normally shows inferior cycling stability and low reversible capacities. The low conductivity and small distance between neighboring layers of MoS_2 materials should be responsible for their poor electrochemical performance. In addition, the MoS_2 nanosheets are prone to agglomeration because of the high surface energy. Because of these issues, the practical application of MoS_2 materials in the energy storage systems has been greatly inhibited.

Compared with MoS_2, $MoSe_2$ exhibits better characteristics for SIBs because of its large interlayer spacing (0.64 nm) and higher electrical conductivity due to the small bandgap, which enables faster charge transfer and improves the electrochemically reversible charge/discharge processes.[19–22] To further improve the electrochemical performance of $MoSe_2$-based materials, coupling with electrically conductive carbon has become a popular approach to improve performances. Chen and co-workers synthesized $MoSe_2$@C@GR nanofibers by electrospinning, which delivered a specific capacity of 366.9 mA h g^{-1} after 200 cycles at 0.2 A g^{-1}.[23] While the simple $MoSe_2$/C composites can raise their electrical conductivity,

H. Liu, Prof. H. Guo, B. Liu, M. Liang, Z. Lv
Yunnan Key Laboratory of Micro/Nano Materials and Technology
School of Materials Science and Engineering
Yunnan University
No. 2, Green Lake North Road, Kunming 650091, China
E-mail: guohongcom@126.com

Prof. H. Guo, Dr. K. R. Adair, Prof. X. Sun
Nanomaterials and Energy Lab
Department of Mechanical and Materials Engineering
Western University
London, Ontario N6A 5B9, Canada
E-mail: xsun9@uwo.ca

The ORCID identification number(s) for the author(s) of this article can be found under https://doi.org/10.1002/adfm.201707480.

DOI: 10.1002/adfm.201707480

they are not capable of buffering the large volume change (up to 300%) during cycling, and thus they usually show poor rate capability.

The development of functional TMDs with well-defined nanostructures is another effective method to improve electrochemical properties. Particularly, the assembly of 3D spatial structures with few layers has several advantages over that of bulk materials and can avoid the problems associated with the rapid aggregation of 2D single-layer nanosheet structures. Among them, encapsulation-type structures have attracted great interest due to their unique structural features, fascinating physicochemical properties, and widespread applications.[24–28] The core in the encapsulation-type structures increases the gravimetric energy density of SIBs through enhancing the weight ratio of the active components. Meanwhile, the void space between the core and shell can effectively buffer large volume expansion of the materials upon cycling and prevents self-aggregation of the nanoscale subunits, which could alleviate the pulverization of active materials and significantly improve the cycling performance. The void structures can also facilitate electrolyte penetration and provide large contact area between the electrode and the electrolyte. Furthermore, the unique structure can decrease the transport distance for sodium ions and electrons, leading to improved rate capability. Wang et al. prepared hollow core–shell iron sulfide-carbon nanospheres used as cathode materials for the emerging sodium-sulfide battery, which exhibited capacity of 545 mA h g^{-1} for over 100 cycles at 0.2 C.[29] The construction of hollow core–shell frameworks is typically associated with template fabrication and multistep/high-cost synthesis, and the hollow structure is often prone to collapse. Therefore, a novel and controllable synthesis design for hollow core–shell encapsulation-type TMDs with high reversible capacity and long cycling life is desirable. Furthermore, it has been discovered that expanding the (002) planes of $MoSe_2$ can enhance the dynamics for sodium-ion intercalation/deintercalation, thus enhancing the sodium storage performance. Zhang and co-workers prepared flower-like $MoSe_2$/C with expanded (002) planes and used it as an anode for SIBs, exhibiting 360 mA h g^{-1} after 350 cycles at 0.5 A g^{-1}.[30] Qiu and co-workers have fabricated carbon-stabilized interlayer-expanded few-layer $MoSe_2$ nanosheets that show a capacity of about 445 mA h g^{-1} after 100 cycles at 1 A g^{-1}.[31] However, most reports show poor capacities, particularly when the current density is higher than 2 A g^{-1}.

Though these procedures are effective, each design strategy alone always leads to limited improvement in the electrochemical properties of TMDs for SIBs. And thus, the development of a facile, scalable, and controllable fabrication of durable hybrid structured TMDs materials with satisfactory cycling ability and high capacity is still highly desired for SIBs. Herein, we design interlayer-expanded few-layer $MoSe_2$ nanosheets spaced-confined in hollow carbon nanospheres (HCNS) to demonstrate our concept and propose a general strategy for the development of such materials, as illustrated in **Scheme 1**. The hollow carbon nanospheres act as nanoreactors and can prohibit the restacking of $MoSe_2$, which enables the formation of uniformly confined few-layer $MoSe_2$ nanosheets with an expanded interlayer spacing structure. The advanced structures improve the sodium-ion intercalation and deintercalation kinetics during cycling and render a more stable capacity. Moreover, the nanostructured hollow anodes exhibit enhanced rate capability and long cycling life.

2. Results and Discussion

2.1. Structure and Morphology of the $MoSe_2$@HCNS Framework

The facile synthesis of the $MoSe_2$@HCNS encapsulation framework is illustrated in Scheme 1. Initially, tetraethylorthosilicate, resorcinol, and formaldehyde aggregate around the SiO_2 core and produce SiO_2@SiO_2/RF core–shell nanostructures. Subsequently, calcination of the product under N_2 at 700 °C leads to the formation of SiO_2@SiO_2/C with a uniform size distribution of ≈250 nm as shown in Figure S1 (Supporting information). In the next step of the fabrication process, a NaOH solution is applied to etch the SiO_2 and form HCNS. The process of generating HCNS with different etching time at 80 °C is shown in Figure S2 (Supporting information). The etching time is an important factor in promoting the formation of uniform HCNS. Finally, the HCNS acts as nanoreactors, resulting in the confined formation of few-layer $MoSe_2$ nanosheets with expanded interlayer spacing. In this process, ethylenediamine ($H_2N{-}CH_2{-}CH_2{-}NH_2$) is used as an intercalating reagent to expand the crystal planes of the few-layer $MoSe_2$ nanosheets. Under hydrothermal conditions, some gases including NH_3 and CO_2 are produced in the system through the addition of ethylenediamine. The rough inner wall of the porous carbon nanospheres is excellent for promoting gas adsorption, resulting in a high concentration of these gases accumulating within the cavity. As a result, the flaky $MoSe_2$ is formed by the reaction of molybdenum source and the selenium source in the cavity of the hollow carbon framework due to the strong force of the gas. Since the flaky $MoSe_2$ is free to diffuse within the hollow structure, the $MoSe_2$ nanosheets are uniformly distributed in the carbon framework. Therefore, hollow carbon nanoreactors play vital roles during this process, and not only provide more active sites for generation of $MoSe_2$ but also promote the confined growth of $MoSe_2$ in the internal carbon shell. In addition, ethylenediamine has another key role as an intercalating reagent to expand the interspacing of $MoSe_2$ layers, where it can restrict the growth of $MoSe_2$ over certain molecular planes such as the (002) plane. Meanwhile, it controls the 2D growth of $MoSe_2$ in the hollow carbon shell frameworks to generate few-layer structures.

The scanning electron microscopy (SEM) images of the prepared SiO_2@SiO_2/C and HCNS are shown in **Figure 1**a,b. It can be seen that the spherical carbon morphology of SiO_2@SiO_2/C can be retained after etching of the SiO_2 and exhibits a shell thickness of about 15 nm. Upon further modification, the space-confined structure $MoSe_2$@HCNS product can be seen in the SEM images of Figure 1c. Furthermore, investigation into the inner structure reveals that petal-like nanosheets are inserted into the cavity of the HCNS, which enables an increase in energy density due the porous structure yielding a higher weight ratio of active components. To confirm the presence of $MoSe_2$ nanosheets within the HCNS, transmission electron

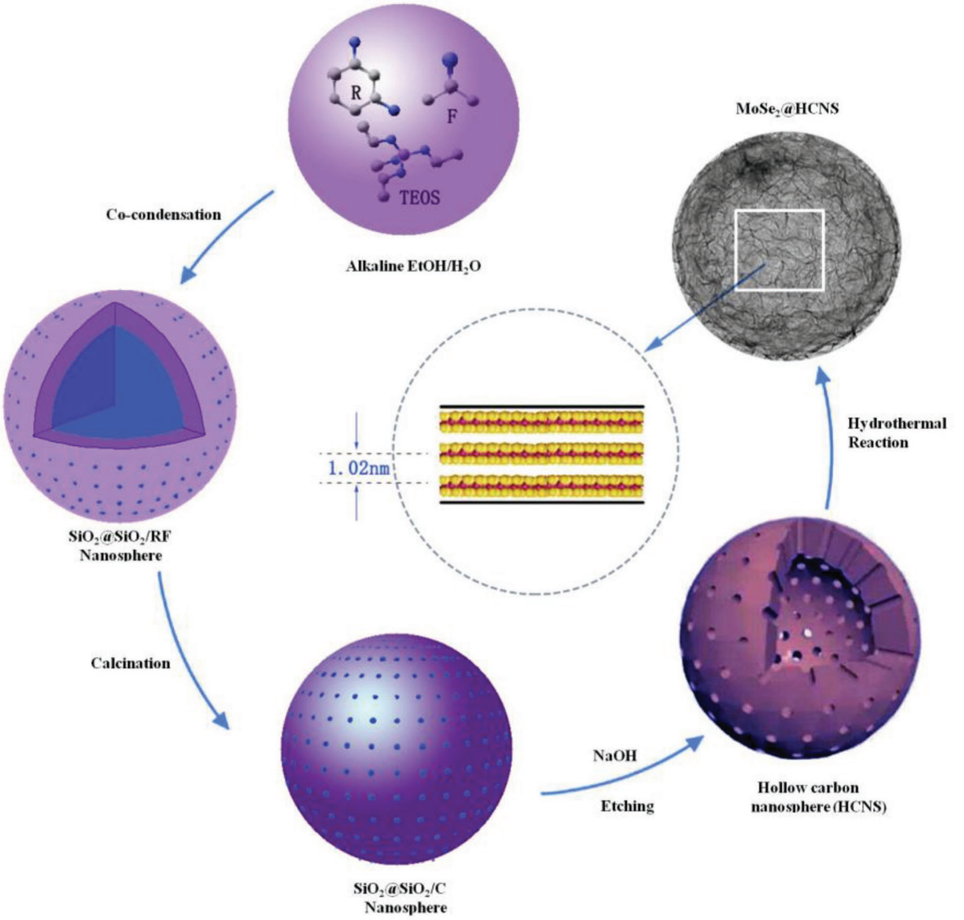

Scheme 1. Representative illustration of the assembly process of encapsulation-type structured MoSe$_2$@HCNS.

microscopy (TEM) was utilized and the images of MoSe$_2$@HCNS are shown in Figure 1d,e, exhibiting thin MoSe$_2$ nanosheets confined in the inner void without obvious aggregation. The selected-area electron diffraction (SAED) pattern (Figure 1e inset) reveals the diffraction rings 1–3 are indexed to (100), (103), and (110) of hexagonal MoSe$_2$ (JCPDS No. 29-0914). The MoSe$_2$@HCNS composite in this study consists of thin isolated MoSe$_2$ strips, while most of the current reports about MoSe$_2$ materials are stacked into aggregates rather than few-layer structures. Remarkably, it was found that our prepared sample exhibits few-layer crystal fringes no more than three layers as displayed in the high-resolution TEM (HRTEM) image of Figure 1f. Therefore, the restriction and stabilization strategies of carbon play a key role in separating and prohibiting the restacking of few-layer MoSe$_2$ nanosheets, leading to improved cycling stability and rate capabilities for SIBs. It is interesting to note that the interlayer spacing of the MoSe$_2$ is expanded to 1.02 nm, which is significantly larger than its intrinsic (002) plane value of 0.64 nm, and can be attributed to the unique effect of the hollow carbon. Moreover, in zone B, the interplanar crystal is expanded to as large as 1.56 nm, in which the increased value (0.54 nm) can be attributed to the sandwiched carbon since the value is smaller than the interlayer spacing. The elemental mapping images (Figure 1g) ascertain the coexistence of Mo and Se, which is uniformly embedded in the hollow layers.

The X-ray diffraction (XRD) analysis patterns of the synthesized encapsulation-type structured MoSe$_2$@ HCNS materials and MoSe$_2$ reference are shown in **Figure 2**a, indicating that the MoSe$_2$@ HCNS material can be matched to hexagonal MoSe$_2$ (JCPDS No. 29-0914). It is found that the molar ratio of Mo/Se in the final products is nearly 0.503 according to quantitative chemical analysis by AAS HITACHI Z-2000, which is in good agreement with the XRD results. The (002) crystal plane peak of carbon at about 26° is attributed to the low content of carbon. To confirm the carbon content of as-prepared MoSe$_2$@HCNS, a typical thermal gravity analysis (TGA) is employed as shown in Figure S3 (Supporting information). The weight loss is attributed to the volatilization of SeO$_2$ and CO$_2$. Based on the TGA data, the calculated carbon content of the MoSe$_2$@HCNS is 8.29 wt%. The pattern of the pure MoSe$_2$ reference prepared without carbon exhibits distinct differences in peak position and intensity for the (002) diffraction peak. The relatively weaker (002) peak of the synthesized yolk–shell MoSe$_2$@HCNS sample indicates restricted growth over the (002) crystal plane and prohibition of multilayer stacking. The interlayer distance of the (002) plane of MoSe$_2$@ HCNS is expanded from 0.64 nm corresponding to pristine MoSe$_2$ to 1.05 nm by calculation

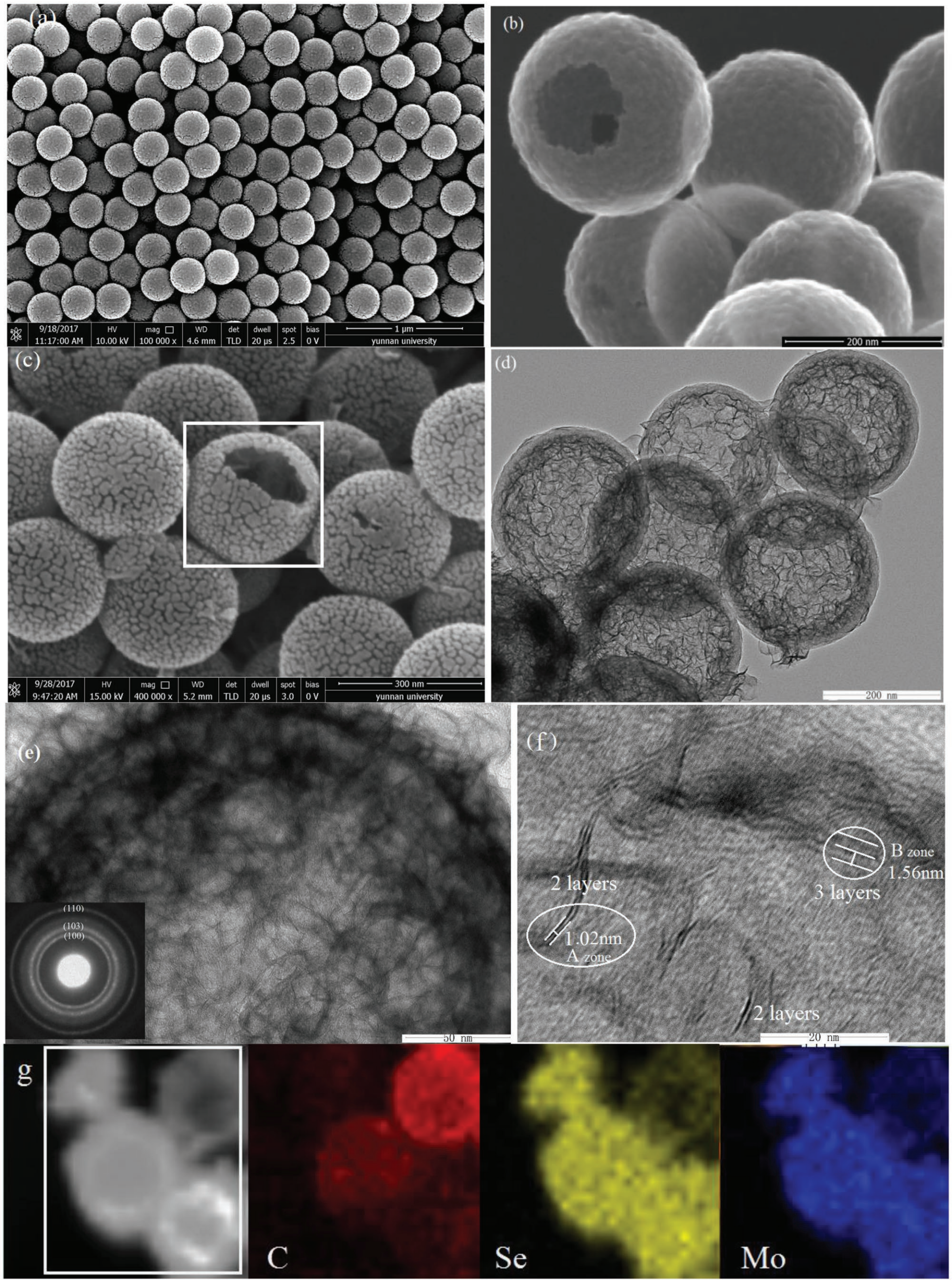

Figure 1. SEM images of the prepared a) SiO_2@ SiO_2/C and b) HCNS; c) SEM, d,e) TEM, and f) HRTEM images of nanostructured $MoSe_2$@HCNS, and SAED (inset in (e)); g) EDX mapping images (the element of C, Se, Mo) of the fabricated $MoSe_2$@HCNS samples.

according to the Scherrer equation. The remarkable increase in interlayer distance can be attributed to the confinement effect of ethylenediamine as a carbon intercalating reagent. Furthermore, in comparison to the pristine $MoSe_2$, the (002) crystal plane of $MoSe_2$@HCNS shifts from 13.2° to 11.4°, suggesting that the interlayer spacing expansion is a result of the carbonization process. These results are in good agreement with the analysis of TEM and HRTEM mentioned above. Therefore, the hollow uniform carbon layers act as crucial role in the confinement and formation of few-layer $MoSe_2$ nanosheets with expanded (002) crystal plane.

The functional groups of the prepared $MoSe_2$@HCNS and HCNS are shown in the Fourier transform infrared spectroscopy (FTIR) spectrum (Figure 2b). The peaks at ≈1640, 1420, 1129, and 776 cm^{-1} of $MoSe_2$@HCNS are a result of the C=O, O—H, C—O, and C—H bonds of organic solutions, respectively.[31,16] The broad absorption peak centered at ≈3447 cm^{-1} is associated with the asymmetric and symmetric stretching vibrations of the —OH group of absorbed water molecules. Furthermore, the weak peak at 1324 cm^{-1} is derived from C—N bonds. The main peaks of the $MoSe_2$@HCNS product are almost the same as those peaks of the HCNS, illuminating

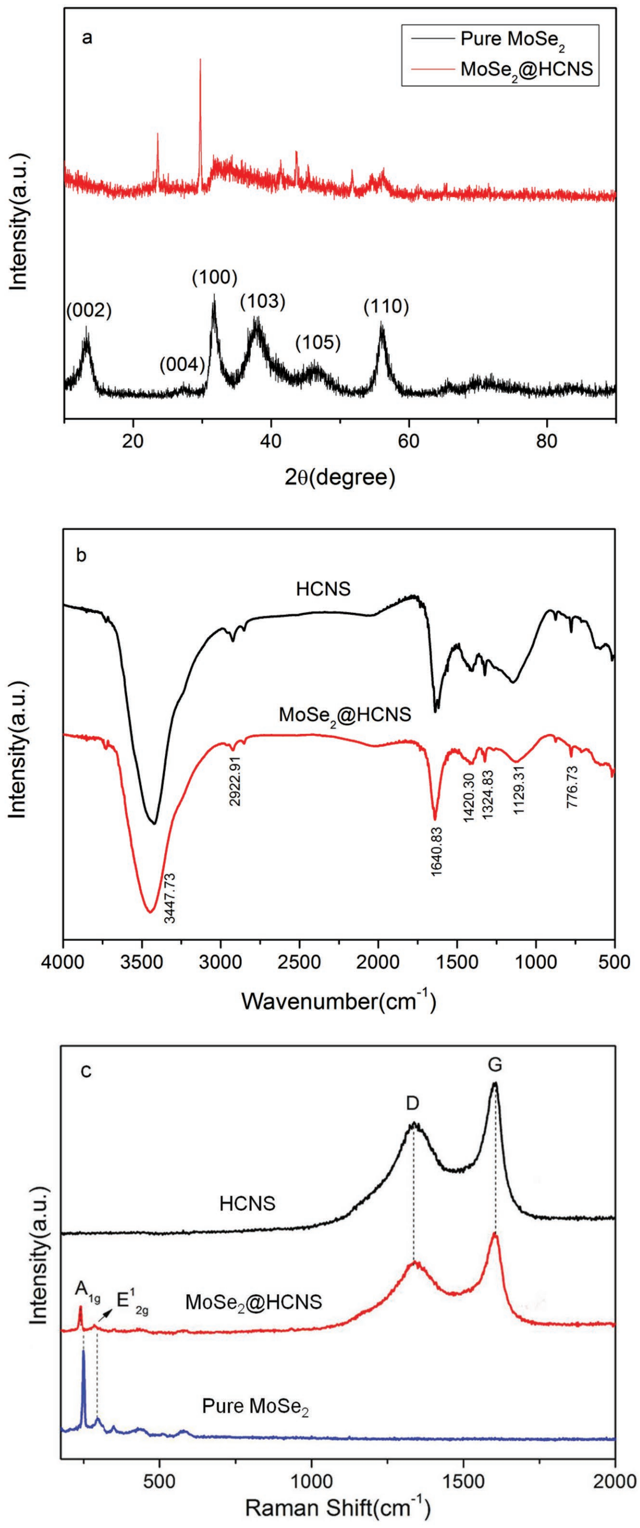

Figure 2. a) XRD patterns of MoSe$_2$@HCNS and MoSe$_2$ reference; b) FTIR spectra of the HCNS and final MoSe$_2$@HCNS product; c) the Raman spectra of HCNS, MoSe$_2$@ HCNS, and pristine MoSe$_2$ reference.

that the generated MoSe$_2$ few-layer nanosheets are distributed in the carbon layers uniformly and also are confined in the space of hollow carbon. Therefore, the FTIR spectrum does not detect different functional group characteristics. To explore the porosity and surface area properties of the MoSe$_2$@HCNS, gas sorption analysis was carried out. The N_2 adsorption/desorption isotherms and the pore size distribution of the obtained MoSe$_2$@HCNS sample are shown in Figure S4 (Supporting information). The adsorption/desorption isotherms are identified as type IV, which is characteristic of mesoporous materials. Furthermore, the average pore diameter of MoSe$_2$@HCNs and HCNs is about 3.829 and 3.877 nm according to the pore size distribution data, respectively. Surface area analysis of the MoSe$_2$@HCNS by the Brunauer–Emmett–Teller (BET) method is 226.31 m^2 g^{-1}, which is smaller than that of the hollow carbon (636.37 m^2 g^{-1} Figure S5, Supporting information). The decrease in BET surface area is likely due to the introduction of MoSe$_2$ nanosheets. In addition, the single-point total pore volume at $P/P_0 = 0.975$ is 0.496 cm^3 g^{-1}. These indicate that the prepared samples have a loose mesoporous structure. Therefore, the special hollow mesoporous architectures are ideal for the accommodation of volume expansion during electrochemical cycling and thus avoid pulverization of the electrode.

According to the Raman spectra (Figure 2c), the D and G bands of the HCNS are located at 1340.71 and 1590.67 cm^{-1}, respectively. Furthermore, the two peaks of the carbon D and G bands in MoSe$_2$@HCNS coincide with the HCNS, confirming the presence of a carbon shell with similar structure. Particularly, the fabricated MoSe$_2$@HCNS have two special Raman characteristic lines due to the insertion of few-layer MoSe$_2$. The abovementioned peaks can be attributed to the Raman active A_{1g} and $E^1{}_{2g}$ modes of MoSe$_2$ located at 239.41 and 284.99 cm^{-1}, respectively, showing an apparent red shift in comparison with the MoSe$_2$ reference. The shift is resulted from the changes in the interlayer spacing and the number of layers according to reports.[23,32] Therefore, the changed character of A_{1g} is a result of signal averaging of the number of MoSe$_2$ nanosheets.

Chemical compositions of these materials are further investigated by X-ray photoelectron spectroscopy (XPS) analysis (**Figure 3**). The survey spectrum shows the existence of C, Mo, Se, and N elements (Figure 3a). The N element is derived from the carbonization of ethylenediamine. The Mo 3d spectrum shows two peaks at 227.8 and 230.9 eV assigned to Mo 3d5/2 and Mo 3d3/2, respectively, indicating the existence of Mo^{4+} (Figure 3b). The peaks at 229.2 and 232.0 eV are attributed to the satellite peaks. The 3d peak of Se^{2-} (Figure 3c) is split into well-defined 3d5/2 and 3d3/2 peaks at 53.8 and 54.2 eV, whereas the C 1s peaks (Figure 3d) at 284.66 and 286.58 eV are ascribed to C—C and C—O, respectively. These results are in good agreement with previous reports.[30,31,33,34]

2.2. Electrochemical Characterizations of MoSe$_2$@HCNS

The electrochemical properties of the nanostructured MoSe$_2$@HCNS as an anode material for SIBs were explored through the use of CR2016 coin cells. The average mass loading of active material was 4.25 mg cm^{-2} and a sodium plate acts as the counter electrode. To study the sodiation mechanism and reversibility of the electrochemical reactions, cyclic voltammetry (CV) was employed using a scan rate of 0.05 mV s^{-1}. The curves for the first three cycles are shown in **Figure 4**a, in

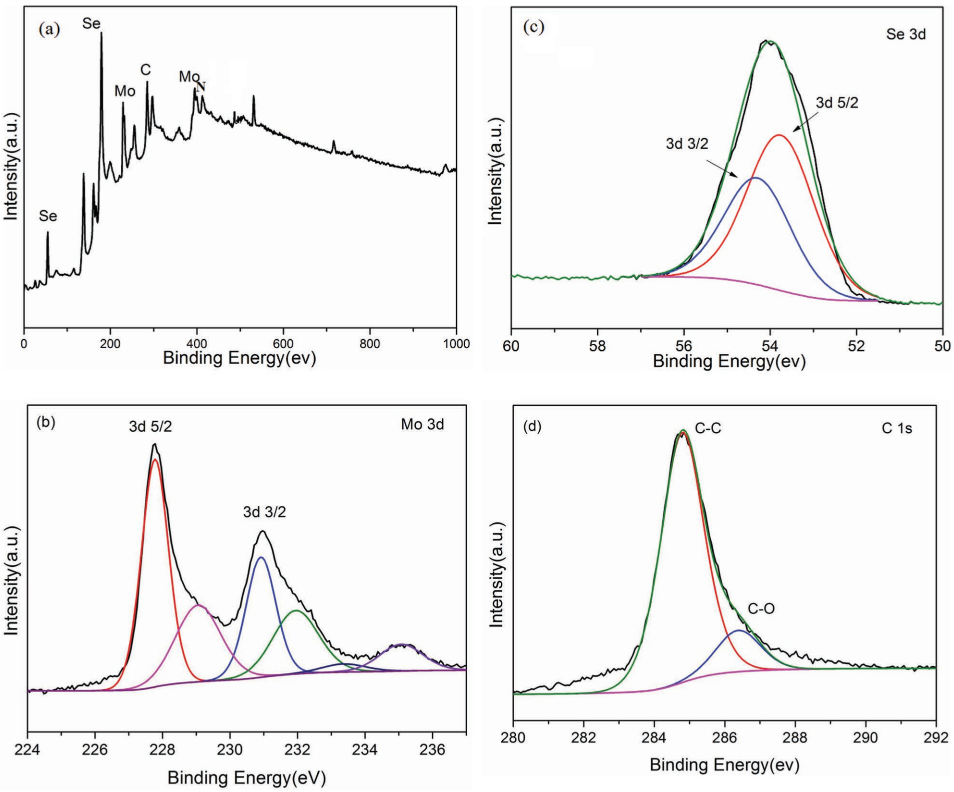

Figure 3. XPS spectra of the as-prepared $MoSe_2$@HCNS: a) survey spectrum, b) Mo 3d, c) Se 3d spectrum, and d) C 1s spectrum.

which the apparent reduction peak at 0.60 V in the first cycle is assigned to the Na^+ insertion into the interlayer of $MoSe_2$ and formation of Na_xMoSe_2, as described by Equation (1).[19] The reduction peak at 0.36 V is ascribed to the conversion reaction from Na_xMoSe_2 to Mo metal and Na_2Se with the formation of a solid electrolyte interphase (SEI) film, as depicted in Equation (2). These peaks disappear in the successive cycles, suggesting the irreversibility of the reaction. This is validated by ex situ XPS and HRTEM measurements according to other previous researches.[20,21] The additional weak reduction peaks at 1.57 and 1.37 V are attributed to the redox of Mo nanoparticles.[35,36] Furthermore, an oxidation peak at 1.72 V is observed, and can be assigned to oxidation of Mo to $MoSe_2$ as described by Equation (3).[31] The discharge branch of the voltammogram for the initial cycle is substantially different from those of the following ones, revealing the occurrence of an irreversible transformation and structure rearrangement. From the second cycle onward, the CV curves overlap very well, demonstrating the good reversibility of the $MoSe_2$@HCNS materials during electrochemical cycling

$$MoSe_2 + xNa^+ + xe^- \rightarrow Na_xMoSe_2 \tag{1}$$

$$Na_xMoSe_2 + (4-x)Na^+ \rightarrow 2Na_2Se + Mo^{4+} \tag{2}$$

$$2Na_2Se + Mo^{4+} \rightarrow MoSe_2 + 4Na^+ \tag{3}$$

The galvanostatic Na^+ intercalation/deintercalation curves of the $MoSe_2$@HCNS electrode at current density of 1 A g^{-1} are shown in Figure 4b, which is in good agreement with the previous CV profiles. According to the first discharge cycle, there is a wide and steady discharging plateau starting at 1.3 V, followed by a gradual voltage decrease. The initial discharge and charge capacities are 912 and 687 mA h g^{-1}, respectively. The initial capacity loss is 226 mA h g^{-1}, which should be attributed to the formation of SEI film and the reduction of metal oxide to metal. The initial coulombic efficiency is 75.32%, which is lower than most reported $MoSe_2$ electrodes.[19–23,30,31] These results are consistent with CV analysis. From the second cycle, the long plateau changes to a long slope from 2.3 to 0.05 V, where a reversible capacity as high as 562 mA h g^{-1} was retained after 100 cycles, exhibiting excellent electrode reversibility. To investigate the effect of the HCNS on the electrochemical properties, the cycling performance of $MoSe_2$@HCNS materials prepared with different etching times by NaOH solution from 0.5 to 4 h is shown in Figure 4c. It can be noticed that specific capacities remarkably increased with the increase of etching reaction time from 0.5 to 2 h. However, the discharge capacity of $MoSe_2$@HCNS corresponding to 4 h is 512 mA h g^{-1} after 150 cycles, which is less than the value of 567 mA h g^{-1} corresponding to that of 2 h, illuminating the electrochemical stability is sensitive to the structure of the $MoSe_2$@HCNS. Therefore, the $MoSe_2$@HCNS used in these studies utilize the hollow carbon with an etching time of 2 h.

Figure 4d exhibits the rate capabilities of the $MoSe_2$@HCNS at different currents from 1 to 10 A g^{-1}. After the 40th cycle at 1 A g^{-1}, the discharge capacity is 562 mA h g^{-1}. When the current density is increased to 3 A g^{-1}, the reversible capacity

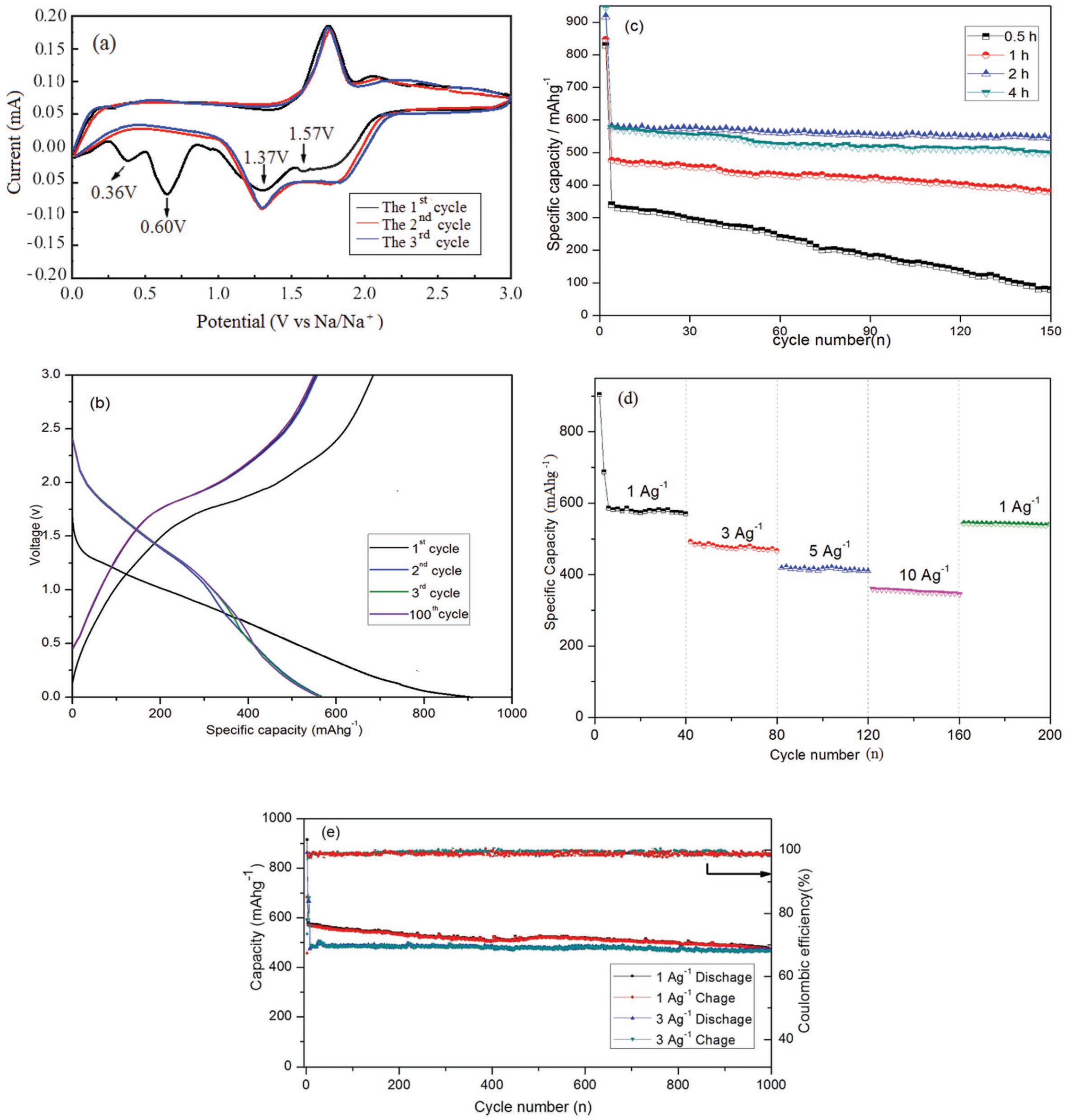

Figure 4. Electrochemical performance of the prepared $MoSe_2$@HCNS for SIBs (electrode potential range of 0.01–3.0 V): a) CV curves with a scan rate of 0.05 mV s^{-1}. b) Charge/discharge curves for the first 3rd and the 100th cycles at current density of 1 A g^{-1}. c) Cycling performance with different etching times ranging from 0.5 to 4 h at a constant current density of 1 A g^{-1}. d) Rate capability of $MoSe_2$@HCNS from 1 to 10 A g^{-1}. e) Cycling capability of $MoSe_2$@HCNS with prolonged cycle life (1000 cycles) at 1 and 3 A g^{-1}.

is still greater than 482 mA h g^{-1} after 80 cycles. Surprisingly, when raising the current density to as high as 10 A g^{-1}, the capacity can still retain 382 mA h g^{-1}. Finally, the capacity recovers to 532 mA h g^{-1} when the current density is reduced to 1 A g^{-1} after 200 cycles. Furthermore, $MoSe_2$@HCNS exhibits excellent stability during electrochemical cycling, even at high current density, which demonstrates its superior reversibility. Notably, the $MoSe_2$@HCNS materials express ultralong cycling life as shown in Figure 4e, from which the discharge capacities are 502 and 471 mA h g^{-1} after 1000 cycles at 1 and 3 A g^{-1}, respectively. Moreover, the Coulombic efficiencies for all the rate performance reach more than 98.3% with the exception of the first cycle. These results show the prepared $MoSe_2$@HCNS anode has superior reversibility and robust stability. It is notable that the capability and long-life cycling performance display significant enhancements compared with other recent reports about anodes for SIBs, such as $MoSe_2$/C/GR,[23] MoSe/CNTs,[37] MoS_2-C,[38] $FeSe_2$,[39] SnS_2,[40] etc., as seen in Table S1 (Supporting Information).The reversible capacity, rate capability, cycling stability, and life of these materials are inferior to the $MoSe_2$@HCNS anode developed in this study. Furthermore, to show that the good electrochemical stability originates from the robust structure of the $MoSe_2$@HCNS anode, TEM images were used to analyze the structure of the sample after 1000 cycles at a current density of 3 A g^{-1} (**Figure 5**). It is interesting to note that the integrated framework of $MoSe_2$@HCNS

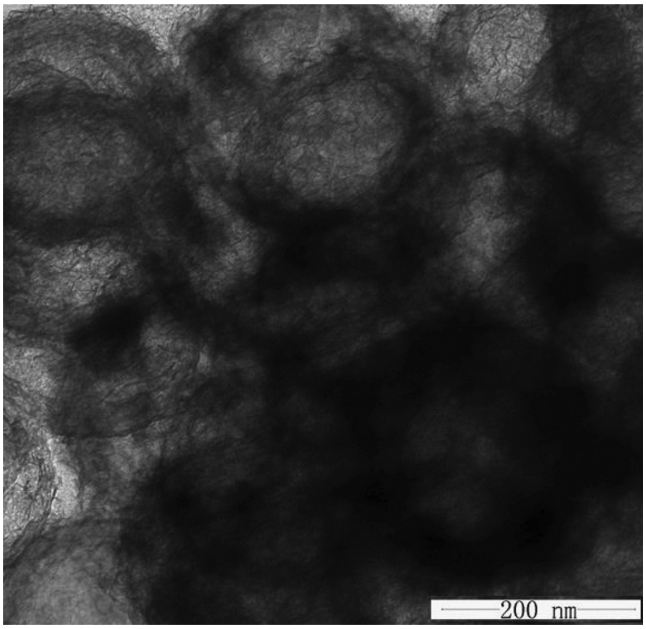

Figure 5. TEM image of $MoSe_2$@HCNS electrode after 1000 cycles at 1 A g^{-1}.

is well maintained without breakage after 1000 cycles during the Na^+ insertion/extraction process.

To further study the effects of the unique structure, electrochemical impedance spectroscopy (EIS) was carried out to analyze the reaction dynamics of $MoSe_2$@HCNS and reference pristine $MoSe_2$ anodes, as shown in **Figure 6**. The semicircle in the medium-frequency band is related to the electrochemical reaction impedance, while the inclined line in the low-frequency zone is related to the solid-state ion diffusion in the electrode bulk. The diameter of the semicircle corresponding to $MoSe_2$@HCNS is obviously smaller than that of the pristine $MoSe_2$ in a fresh cell system, revealing the charge transfer efficiency of $MoSe_2$@HCNS is increased significantly. Meanwhile, the ionic conductivity is also improved, as shown by the slope of the profile in the low-frequency region. Furthermore, the Ohmic resistance (R_s) of $MoSe_2$@HCNS is simulated as 3.2 Ω, which is lower than that of the pristine $MoSe_2$ (9.3 Ω). The calculated charge-transfer resistance (R_{ct}) of $MoSe_2$@HCNS is 115.8 Ω, which is also lower than that of the pristine $MoSe_2$ (568.7 Ω). The small Warburg impedance of $MoSe_2$@HCNS is attributed to the enhanced ion diffusion in the few-layer $MoSe_2$ with expanded interlayer spacing, leading to greater ionic conductivities. Thus, the hollow carbon structure and the introduction of ethylenediamine play a key role in achieving enhanced Na^+ storage properties. The HCNS structure can shorten the length of Na^+ diffusion, which benefits the rate performance. Furthermore, the hollow structure offers sufficient void space capable of alleviating the mechanical stress caused by the volume change of $MoSe_2$ during the intercalation/deintercalation process. Additionally, the few-layer nanosheets enhance the permeation of electrolyte into the inner part of active materials, thus increasing the contact zone, and leading to greater ionic and electronic conductivities. Therefore, the $MoSe_2$@HCNS electrode exhibits excellent electrochemical performance.

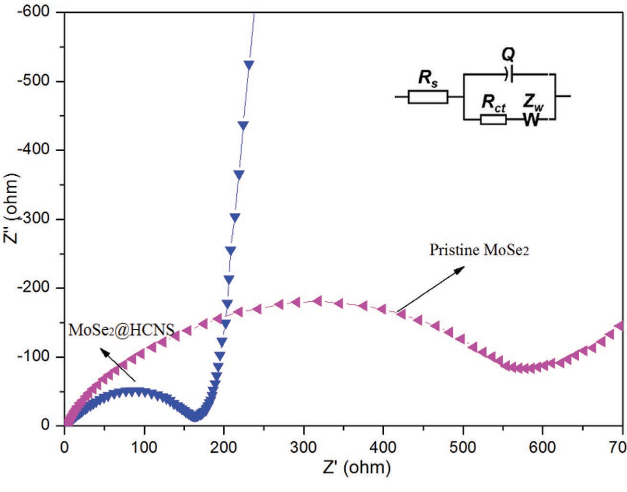

Figure 6. EIS spectra of $MoSe_2$@HCNS and $MoSe_2$ reference before cycling and the equivalent circuit (inset).

3. Conclusions

In summary, few-layer $MoSe_2$ nanosheets with expanded (002) planes are successfully confined within the cavity of hollow carbon nanospheres and form a high-performance hybrid $MoSe_2$@HCNS material. The $MoSe_2$ exhibits few-layer crystal fringes no more than three layers and the interlayer spacing is expanded to 1.02 nm. When applied as an anode in SIBs, the $MoSe_2$@HCNS materials exhibit prolonged cycling life with discharge capacities of 502 and 471 mA h g^{-1} after 1000 cycles at 1 and 3 A g^{-1}, respectively. Notably, the Coulombic efficiencies for all the tested rate performances reach more than 98.3%. Even when the current density is raised to as high as 10 A g^{-1}, the capacity can retain 382 mA h g^{-1}, and the capacity recovers to 532 mA h g^{-1} when the current density reduces to 1 A g^{-1} after 200 cycles. Such superior prolonged cycling life and high rate capacity are attributed to the unique carbon-stabilized $MoSe_2$@HCNS hybrid framework, expanded (002) crystal planes, and few-layer $MoSe_2$ nanosheet structure. These attributes improve the transfer efficiency of the electrons and ions, enhances the electrical conductivity, buffers the volume change, and promotes the reversible desodiation–sodiation of the $MoSe_2$@HCNS anode. Therefore, the $MoSe_2$@HCNS displays great potential for application in SIBs. This general strategy can also be further applied to explore other advanced materials used in energy and environmental science.

4. Experimental Section

Materials: Ethanol, NaOH, resorcinol, formaldehyde, ethylenediamine, tetraethylorthosilicate, ammonia solution (25 wt%), Na_2MoO_4, and selenium and hydrazine hydrate ($N_2H_4H_2O$, 80%) solution were all analytical grade and were used without further purification. Water used was purified using an Ulu-pure system (Shanghai China).

Synthesis of Hollow Mesoporous Carbon Spheres: 70 mL of ethanol, 10 mL of H_2O, and 3 mL of ammonia solution (25 wt%) were stirred vigorously to form homogeneous solution. Then 3.46 mL tetraethylorthosilicate and 5 mL ethylenediamine were added to the solution stirring for 15 min. 0.4 g resorcinol and 0.56 mL formaldehyde were added and stirred for 24 h sequentially at room temperature to form the SiO_2@SiO_2/RF core–shell structured nanospheres. Second, the obtained precipitates were separated by centrifugation, washed with deionized water and ethanol, followed by drying under vacuum at 60 °C overnight. Later, the precipitates were calcined under N_2 to 700 °C (2 °C min^{-1}) for 5 h to obtain the SiO_2@SiO_2/C nanospheres. Finally, the HCNS were obtained by removing silica using sodium hydroxide (NaOH, 2 M). The product was also obtained by centrifugating and washed with deionized water before being dried at 60 °C overnight.

Synthesis of $MoSe_2$@HCNS: 0. 2 mmol Na_2MoO_4 was dispersed in 50 mL distilled water under constant stirring to form a clear solution. Separately, 0.4 mmol selenium was dissolved in 10 mL hydrazine hydrate ($N_2H_4H_2O$, 80%) solution and stirred for 5 h, where the colorless solution instantly turns dark brown. Then 10 mL hydrazine hydrate-Se was added to 50 mL Na_2MoO_4 and slowly stirred for 30 min, followed by dissolving 20 mg of HCNS into the solution. After ultrasonic dispersion for 1 h, the mixture was transferred to a 100 mL Teflon-lined autoclave and heated in an oven at 200 °C for needed time. The solution was transferred out for centrifugation. The products were washed with deionized water and ethanol before being dried at 60 °C in vacuum overnight. Finally, the as-prepared sample was treated at 500 °C for 5 h to obtain well-crystallized $MoSe_2$@HCNS composites. Characterization and electrochemical measurement are shown in the Supporting Information.

Supporting Information

Supporting Information is available from the Wiley Online Library or from the author.

Acknowledgements

H.L., B.L., and M.L. contributed equally to this work. The authors would like to acknowledge financial support provided by National Natural Science Foundation of China (Nos. 51474191 and 21467030), Natural Science Key Foundation of Yunnan Province China (Nos. 2018FA001 and 201701PE00011), Major State Basic Research Development Program of China (973 Program, No. 2014CB643406), and the Program for Excellent Young Talents, Yunnan University.

Conflict of Interest

The authors declare no conflict of interest.

Keywords

encapsulation-type structure, few-layer $MoSe_2$ nanosheets, sodium-ion batteries, ultralong cycling life

Received: December 25, 2017
Revised: February 5, 2018

---

[1] J. B. Goodenough, K. S. Park, *J. Am. Chem. Soc.* **2013**, *135*, 1167.
[2] H. S. Li, Y. Ding, H. J. H, Y. Shi, L. L. Peng, X. G. Zhang, C. J. Ellison, G. H. Yu, *Adv. Mater.* **2017**, *29*, 1700898.
[3] Y. Sun, J. Tag, K. Zhang, J. Yuan, J. Li, D. M. Zhu, K. Ozawa, L. C. Qin, *Nanoscale* **2017**, *9*, 2585.
[4] X. Song, X. Li, Z. Bai, B. Yan, D Li, X. Sun, *Nano Energy* **2016**, *26*, 533.
[5] X. Liu, Y. W. Wang, Z. Y. Wang, T. Zhou, M. Z. Yu, L. Y. Xiu, J. S. Qiu, *J. Mater. Chem. A* **2017**, *5*, 10398.
[6] S. Wang, L. Xia, L. Yu, L. Zhang, H. Wang, X. W. Lou, *Adv. Energy Mater.* **2016**, *6*, 1502217.
[7] M. D. Slater, D. Kim, E. Lee, C. S. Johnson, *Adv. Funct. Mater.* **2013**, *23*, 947.
[8] K. F. Mak, J. Shan, *Nat. Photonics* **2016**, *10*, 216.
[9] Y. Cai, H. Yang, J. Zhou, Z. Luo, G. Fang, S. Liu, A. Pan, S. Liang, *Chem. Eng. J.* **2017**, *327*, 522.
[10] C. B. Zhu, X. K. Mu, P. A. V. Aken, Y. Yu, J. Maier, *Angew. Chem., Int. Ed.* **2014**, *53*, 2152.
[11] Q. Pang, Y. Gao, Y. Zhao, Y. Ju, H. Qiu, Y. Wei, B. Liu, B. Zou, F. Du, G. Chen, *Chemistry* **2017**, *23*, 7074.
[12] S. Mouri, W. Zhang, D. Kozawa, Y. Miyauchi, G. Eda, K. Matsuda, *Nanoscale* **2017**, *9*, 6674.
[13] S. Deng, Y. Zhong, Y. Zeng, Y. Wang, Z. Yao, F. Yang, S. Lin, X. Wang, X. Lu, X. Xia, J. Tu, *Adv. Mater.* **2017**, *29*, 1700748.
[14] W. Sun, P. Li, X. Liu, J. Shi, H. Sun, Z. Tao, F. Li, J. Chen, *Nano Res.* **2017**, *10*, 2210.
[15] Y. L. Ding, P. Kopold, K. Hahn, P. A. V. Aken, J. Maier, Y. Yu, *Adv. Mater.* **2016**, *28*, 7774.
[16] H. Jiang, D. Ren, H. Wang, Y. Hu, S. Guo, H. Yuan, P. Hu, L. Zhang, C. Li, *Adv. Mater.* **2015**, *27*, 3687.
[17] Z. Hu, L. Wang, K. Zhang, J. Wang, F. Cheng, Z. Tao, J. Chen, *Angew. Chem.* **2014**, *126*, 13008.
[18] X. Zhang, R. Zhao, Q. Wu, W. Li, C. Shen, L. Ni, H. Yan, G. Diao, M. Chen, *ACS Nano* **2017**, *11*, 8429.
[19] Y. N. Ko, S. H. Choi, S. B. Park, Y. C. Kang, *Nanoscale* **2014**, *6*, 10511.
[20] D. Xie, W. Tang, Y. Wang, X. Xia, Y. Zhong, D. Zhou, D. Wang, X. Wang, J. Tu, *Nano Res.* **2016**, *9*, 1618.
[21] H. Wang, X. Wang, L. Wang, J. Wang, D. Jiang, G. Li, Y. Zhang, H. Zhong, Y. Jiang, *J. Phys. Chem. C* **2015**, *119*, 10197.
[22] H. Wang, X. Lan, D. Jiang, Y. Zhang, H. Zhong, Z. Zhang, Y. Jiang, *J. Power Sources* **2015**, *283*, 187.
[23] C. Cui, G. Zhou, W. Wei, L. Chen, C. Li, J. Yue, *J. Alloys Compd.* **2017**, *727*, 1280.
[24] H. Guo, L. Liu, T. Li, W. Chen, Y. Wang, W. Wang, *Chem. Commun.* **2014**, *50*, 673.
[25] Y. J. Hong, M. Y. Son, Y. C. Kang, *Adv. Mater.* **2013**, *25*, 2279.
[26] H. Guo, R. Mao, D. Tian, W. Wang, X. Yang, S. Wang, *J. Mater. Chem. A* **2013**, *1*, 3652.
[27] L. Yu, B. Y. Guan, W. Xiao, X. W. Lou, *Adv. Energy Mater.* **2015**, *5*, 1500981.
[28] H. Guo, L. Liu, T. Li, W. Chen, J. Liu, Y. Guo, Y. Guo, *Nanoscale* **2014**, *6*, 5491.
[29] Y. X. Wang, J. P. Yang, S. L. Chou, H. K. Liu, W. X. Zhang, D. Y. Zhao, S. X. Dou, *Nat. Commun.* **2015**, *6*, 8689.
[30] J. Li, H. X. Hu, F. R. Qin, P. Zhang, L. Zou, H. B. Wang, K. Zhang, Y. Q. Lai, *Chem. Eur. J.* **2017**, *23*, 14004.
[31] Y. Tang, Z. Zhao, Y. Wang, Y. Dong, Y. Liu, X. Wang, J. Qiu, *ACS Appl. Mater. Interfaces* **2016**, *8*, 32324.
[32] H. Tang, K. Dou, C. Kaun, Q. Kuang, S. Yang, *J. Mater. Chem. A* **2014**, *2*, 360.
[33] M. Minakshi, M. J. Barmi, R. T. Jones, *Dalton Trans.* **2017**, *46*, 3588.
[34] M. J. Barmi, M. Minakshi, *ChemPlusChem* **2016**, *81*, 964.
[35] X. Zhou, L. J. Wan, Y. G. Guo, *Chem. Commun.* **2013**, *49*, 1838.
[36] Q. Wang, J. Li, *J. Phys. Chem. C* **2007**, *111*, 1675.
[37] Z. Zhang, X. Yang, Y. Fu, K. Du, *J. Power Sources* **2015**, *296*, 2.
[38] Z. T. Shi, W. Kang, J. Xu, Y. W. Sun, M. Jiang, T. W. Ng, H. T. Xue, D. Y. W. Yu, W. Zhang, C. S. Lee, *Nano Energy* **2016**, *22*, 27.
[39] X. J. Wei, C. J. Tang, Q. Y. An, M. Y. Yan, X. P. Wang, P. Hu, X. Y. Cai, L. Q. Mai, *Nano Res.* **2017**, *10*, 3202.
[40] W. Sun, X. Rui, D. Yang, Z. Sun, B. Li, W. Zhang, Y. Zong, S. Madhavi, S. Dou, Q. Yan, *ACS Nano* **2015**, *9*, 11371.